ELSEVIER

Contents lists available at ScienceDirect

Sensors and Actuators: A. Physical

journal homepage: www.journals.elsevier.com/sensors-and-actuators-a-physical





GMR biosensing with magnetic nanowires as labels for the detection of osteosarcoma cells

Diqing Su^a, Joseph Um^b, Julian Moreno^c, Zohreh Nemati^b, Karthik Srinivasan^b, Junyang Chen^b, M. Reza Zamani Kouhpanji^b, Daniel Shore^a, Kai Wu^b, Jürgen Kosel^c, Jaime F. Modiano^{d,e,f,g,h,i}, Rhonda Franklin^{b,i}, Jian-Ping Wang^{a,b,f,i,*}, Bethanie Stadler^{a,b,f,i,*}

- ^a Department of Chemical Engineering and Materials Science, University of Minnesota, Minneapolis, MN 55455, USA
- ^b Department of Electrical and Computer Engineering, University of Minnesota, Minneapolis, MN 55455, USA
- ^c Electrical Engineering Department, King Abdullah University of Science and Technology, Thuwal 23955, Saudi Arabia
- ^d Animal Cancer Care and Research Program, University of Minnesota, St. Paul, MN 55108, USA
- ^e Department of Veterinary Clinical Sciences, College of Veterinary Medicine, University of Minnesota, St. Paul, MN 55108, USA
- f Masonic Cancer Center, University of Minnesota, Minneapolis, MN 55455, USA
- g Center for Immunology, University of Minnesota, Minneapolis, MN 55455, USA
- ^h Stem Cell Institute, University of Minnesota, Minneapolis, MN 55455, USA
- ¹ Institute for Engineering in Medicine, University of Minnesota, Minneapolis, MN 55455, USA

ARTICLE INFO

Keywords: Giant magnetoresistance (GMR) Biosensors Magnetic nanowires Cell detection Angular dependence

ABSTRACT

Magnetic nanowires (MNWs) were explored as potential magnetic tags for cell detection with giant magnetoresistance (GMR) biosensors based on a handheld system. Due to size, shape anisotropy and higher moment materials, the signal detected from a single MNW was 2500 times larger than that from a single magnetic iron oxide nanobead, which is important for ultra-low concentration cell detection. A model was used to determine how the MNW orientation with respect to the GMR sensor impacts detection performance, and the results aligned well with the experimental results. As a proof of concept OSCA-8 cells tagged with Ni MNWs were also detected using the same handheld system. The limit of detection (LOD) in aqueous solution appeared to be 133 cells, and single-cell detection can be realized if the cell is in direct contact with the sensor surface. Since MNWs are already employed in magnetic separation of cells, directly using MNWs as tags in cell detection eliminates the need of additional functionalization with other labels. This largely simplifies the detection process and reduces the risk of contamination during sample preparation.

1. Introduction

To fulfill the growing demand for rapid and sensitive diagnosis of various biomarkers, the development of cutting-edge point-of-care devices has become an important research topic for electrical and biomedical engineers. The most widely used optical [1,2] and plasmonic [3,4] sensors often require additional amplification techniques, such as polymerase chain reaction (PCR), to increase the number of target analytes [5,6], and this increases both the cost and the complexity of the detection process. Optical and plasmonic signals can also be influenced by the chemical environment of the biological sample, which leads to variation of sensitivity and poor reliabilities if the detection is performed in more complexed biological environments like blood, urine or nasal

swab samples. As an alternative approach, magnetic biosensors are only sensitive to the magnetic signal from the magnetic tags attached to the target molecule. Since most of the components in the sample matrix are nonmagnetic, magnetic sensors exhibit much lower background noise [7,8]. The possibility of using giant magnetoresistance (GMR) sensors in biomarker detection was first explored in 1998 [9]. While there has been much effort to improve the sensing scheme from the sensor side [7, 10–15], the magnetic nanoparticles (MNPs) used in the detection process haven't changed much except for the optimization of the particle diameter and the magnetic material [16,17]. However, the sensitivity of biological detection is intrinsically limited by the magnetic moment of the MNPs. With the growing demand for the detection of ultra-low-concentration biomarkers to achieve early diagnosis, new

^{*} Corresponding authors at: Department of Chemical Engineering and Materials Science, University of Minnesota, Minneapolis, MN 55455, USA *E-mail addresses*: jpwang@umn.edu (J.-P. Wang), stadler@umn.edu (B. Stadler).

types of magnetic nanotags with high magnetic moment and biocompatibility will be crucial to further improve the sensitivity of the magnetic biosensor systems.

One candidate that can meet both of the requirements is the magnetic nanowire (MNW), which has already been employed in many biological applications such as drug delivery [18,19], cancer treatment by magneto-mechanical effect [20] often in combination with targeted drug delivery, cell manipulation and magnetic separation [21], as well as biosensing [22]. Like magnetic nanobeads, MNWs can also be functionalized with biomolecules such as polyethylene glycol [23], peptides [24], glycoproteins, and DNA [25]. Compared to a MNP made with the same material, a MNW exhibits much higher magnetic moment due to larger size and shape anisotropy. MNWs are biocompatible, although as with all nanomaterials this depends on the material, dose and treatment [26], and MNWs are readily internalized by cells [27]. Whether detecting MNPs or MNWs, there is negligible background noise in either buffer solutions or complex sample matrices due to the non-magnetic nature of bioenvironments. It can be foreseen that by replacing MNPs with MNWs, the sensitivity of the GMR magnetic sensing system can be largely improved. Unlike MNPs, MNWs can be synthesized with multi-layered structures [28,29] for multiple biomarkers and unique magnetic signatures. Furthermore, with MNWs as tags, it is possible that GMR sensing can evolve from molecular level detection [7] only to both molecular and cellular level detection.

Here, we aim to explore the possibility of employing nickel (Ni) MNWs as the tags in the GMR biosensing process. Using our handheld GMR sensing system [30,31], the sensor signal generated by the settlement of MNWs on the sensor surface can be recorded. The influence of MNW-to-sensor distance, the number of MNWs and the orientation of the MNWs will be discussed. Most of the stray fields from MNWs come from their ends, which means variations in MNW shape and length cause negligible impact on sensing. Although the detection of MNWs with GMR sensors has been reported in microfluidics [32], the readout of large volumes of analytes is prohibitively slow, especially when only small numbers of MNWs are present. The focus of this paper is on the detection of low cell concentrations via magnetic purification of the cells, which then settle onto the sensor. These mechanisms are efficient in large analytes and demonstrate the potential of MNWs as nanotags for ultra-low-concentration cell detection, canine osteosarcoma cells (OSCA-8), which are derived from a tumor sample taken from the left shoulder of a two-year-old male Rottweiler dog with confirmed diagnosis, were employed as the target analytes since they have been widely used as the subject of cancer research. The capability of the detection of cancer cells such as OSCA-8 demonstrates the great potential of our platform in the business of early cancer diagnosis.

2. Experimental section

2.1. GMR sensor fabrication

GMR stacks with a spin valve structure of Ta (5 nm)/NiFe (2 nm)/ CoFe (1 nm)/Cu (3 nm)/CoFe (2 nm)/IrMn (8 nm)/Ta (5 nm) were deposited on Si/SiO2 wafers by magnetron sputter deposition. To achieve a linear response with external field, the sensor area was defined as several stripes with high aspect ratios via photolithography and ion milling. There were 24 stripes in each GMR sensor. Each stripe was 150 μm long and 750 nm wide, and they were connected by Au electrodes. The sensor surface was then passivated with either 18 nm Al₂O₃ and 15 nm SiO₂ or with 500 nm SiO₂. After microfabrication, each wafer was cut into 25 chips. There were two sensor arrays per chip, each of which contained 29 GMR sensors. The chips were annealed at 200 °C for 1 hr under a magnetic field of 5000 Oe (398 kA/m) along the short axes of the sensor strips. The typical response of GMR sensor resistance in response to an applied magnetic field is shown in Fig. S1. The MR ratio of the sensor was \sim 1% under a magnetic field between - 30 Oe (-2.39 kA/m) and 30 Oe (2.39 kA/m).

2.2. Synthesis of MNWs

Ni nanowires were fabricated by electrochemical deposition at room temperature into anodic aluminum oxide (AAO) templates purchased from InRedox LLC, which had honeycomb-like structures consisting of uniform pores (120 nm in diameter). The Ni electrolyte was a mixture of nickel sulfate, nickel chloride, and boric acid. The pH of the solution was adjusted to 4.5 by adding the diluted NaOH. Prior to the electrodeposition, Ti (7 nm) and Cu (200 nm) films were sputtered on the one side of AAO as an adhesion layer and an electric contact for electrodeposition, respectively. The length of nanowires was about 33 μ m, controlled by monitoring the deposited charge. The length was confirmed with JEOL 6500 scanning electron microscopy (SEM) and energy-dispersive X-ray spectroscopy (EDS), as shown in Fig. 1(a) and (b), respectively. Next, the AAO was dissolved in 1 M NaOH to free Ni MNWs, followed by three iterations of magnetic collection and rinsing in deionized water. The rinsed Ni nanowires were kept in ethanol for preservation.

2.3. MNW detection with GMR sensors

For MNW detection, two reaction wells were assembled on top of the two sensor arrays in the GMR chip (Fig. 1(c)) using PDMS (Fig. 1(d)). The chip was then baked at 75 °C for 8 min for the PDMS to dry. These chips were then inserted into a handheld system for read out (Fig. 1(e)). A detailed description of this system can be found in Ref. [29]. The baseline magnetoresistance (MR) value for each of the 29 sensors in the sensor array was measured under a magnetic field between - 30 Oe $(-2.39\ kA/m)$ and 30 Oe $(2.39\ kA/m)$. Next, 30 μL Ni MNW solution was added to each reaction well. To calibrate the signal before cell studies, the MNWs were suspended in ethanol so that the solvent evaporated quickly, minimizing the MNW movement on the sensor surface. The sensor signal (S) was defined as follows:

$$S = \frac{MR - MR_0}{MR_0} \tag{1}$$

where MR andMR₀ are the magnetoresistance after and before the addition of MNWs, respectively. The sensor signal was expressed in parts per million (ppm). The final MR for each GMR sensor was taken as the average of the last 5 min of the saturated signal, and the initial MR was taken as the average of the baseline. After the signal acquisition, the reaction wells were removed so that the MNW number and distribution on each sensor could be characterized by a JOEL 6700 SEM. Reaction wells were not used in the angular dependence measurements to obtain a cleaner sensor surface, which will be discussed in session 3.2.

2.4. Preparation of OSCA-8 cells with MNW labels

The Ni MNWs were functionalized in 0.5 M NaCl solution containing 1 mg PEG/mg Ni at pH \sim 13 for 24 hr at 4 °C, followed by rinsing and sonication in PBS. Simultaneously, 10⁶ canine OSCA-8 cells were incubated for 18 h in OSCA medium. This medium contains Dulbecco's Modified Eagle Medium (DMEM) with high glucose [GIBCO11965] supplemented with 10% fetal bovine serum (FBS), 0.2% Primocin (Invivogen), and 1% 4-(2-hydroxyethyl)- 1-piperazineethanesulfonic acid (HEPES). The propagated cells (3 $\times 10^5$) were then placed into each well of a 6-well plate, followed by another 18 h incubation in OSCA medium. Next, 30 µg Ni MNWs were added to each well, followed by another 48-hour incubation. Unattached MNWs were washed away, the cells were detached from the bottom of the petri dish with trypsin, and the sample was poured into a vial. An external magnet was held to the side of the vial for several minutes to collect MNW-labelled cells, and the medium was poured out and replaced by PBS for re-dispersal by sonication. This was done three times to rinse magnetically collected cells of other debris. Finally, the cells were fixed with a mixture of 2.5% Glutaraldehyde and 0.1 M Cacodylate for 50 min, rinsed 3x with 0.1 M

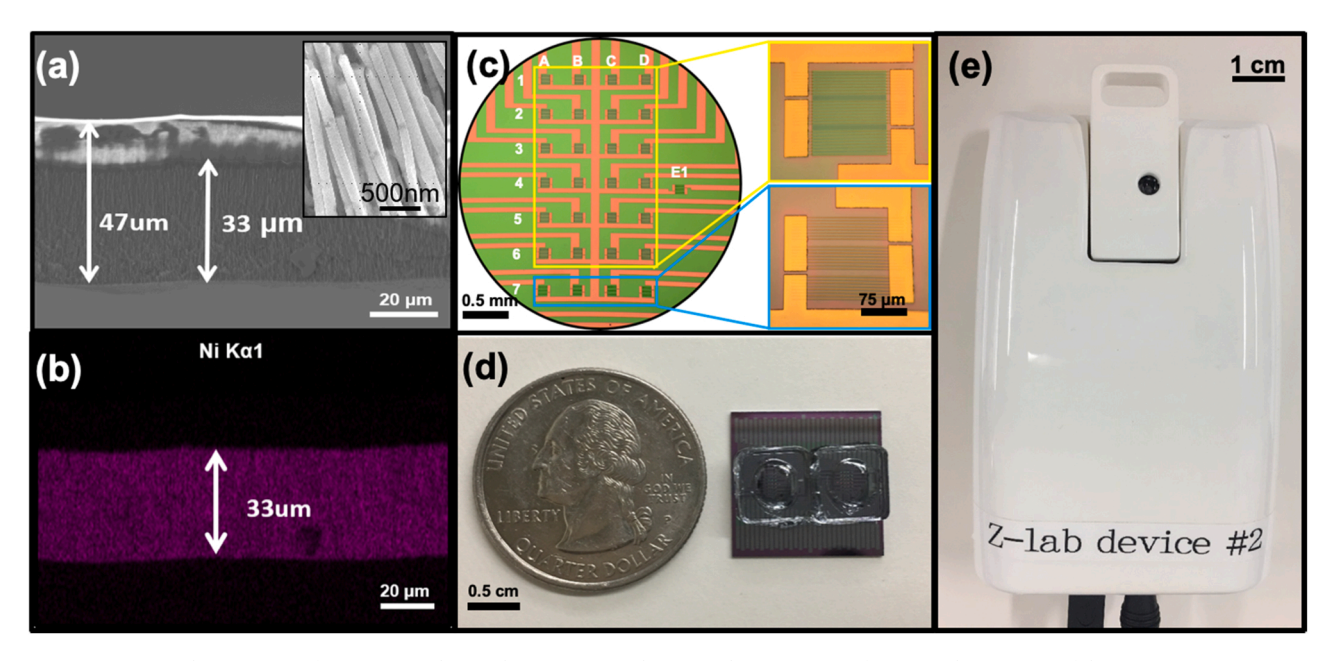


Fig. 1. (a) Cross-sectional SEM image of an AAO template with Ni MNWs inside (inset: close-up image of MNWs). (b) EDS map of the SEM image in (a). (c) Optical microscope image of one sensor array on the GMR chip. There are 29 GMR sensors in each array. The top 24 sensors in the yellow region were passivated with 18 nm Al_2O_3 and 15 nm SiO_2 and the bottom 4 sensors in the blue region were passivated with 500 nm SiO_2 . No passivation layer was deposited on the individual sensor (E1) on the right side of the array. Insets show individual sensorsvfrom the yellow and blue regions, respectively. (d) Photograph of the GMR sensor chip with two reaction wells on it. (e) Photograph of the GMR handheld system. The GMR chips were inserted in the cartridge in the top part of the image.

sodium cacodylate, and dehydrated in ethanol.

3. Results and discussion

In spin valve sensors, such as the sensors used here, the

magnetization direction of the pinned layer is fixed along the short axes of the sensor stripes by the annealing process (horizontal direction in Fig. 2(a)), while the magnetization direction of the free layer is along the long axis of the stripe due to shape anisotropy (vertical direction in Fig. 2 (a)). This perpendicular arrangement results in a linear resistance

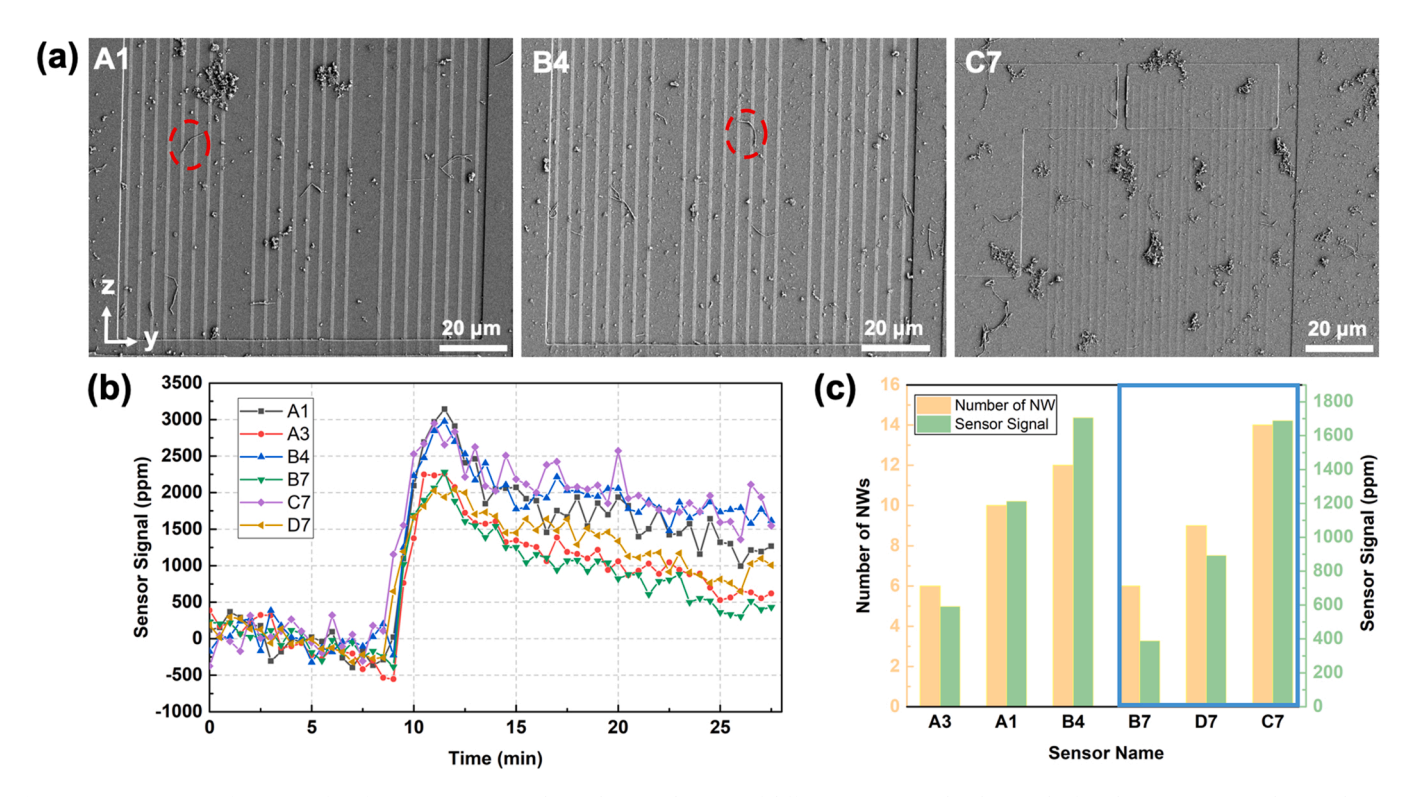


Fig. 2. (a) SEM images of sensor surface for sensor A1, B4, and C7. The exact location of different sensors on the chip can be found in Fig. 1(c). Y and Z axis denotes the direction of the short axis and the long axis of the GMR sensor stripe, respectively. (b) Real-time sensor signal for the six sensors with well-dispersed MNWs. (c) Relationship between number of MNWs on the sensor surface and the detected sensor signal. Sensors within the blue box were passivated with 500 nm SiO_2 while other sensors were passivated with 18 nm Al_2O_3 and 15 nm SiO_2 .

change in response to external magnetic fields (Fig. S1). As the MNWs landed on the sensor surface, the stray fields from the MNWs changed the effective magnetic field experienced by the sensors, which led to a variation in the magnetoresistance. Like most of the commonly used magnetic tags in biomarker detection, the sensor signal induced by the MNWs can be determined by multiple factors, including the magnetic material, the distance between the magnetic tags and the sensor surface, and the number of the captured magnetic tags. In addition, due to the highly anisotropic nature of MNWs, the angles between the MNWs and sensor stripes also contribute to the acquired signal. In this section, the effects of all the aforementioned factors will be investigated and discussed to illustrate both the potential and the challenge in employing MNWs as the tags for GMR-based biomarker detection.

3.1. Detection of Ni MNWs with GMR sensors

Ni MNWs were dissolved in ethanol and sonicated for 5 min before they were added to the reaction wells. Even though the solvent evaporated within several minutes, the aggregation of MNWs was observed for some of the sensors (Fig. S2). As described in the Experimental section, prior to characterizing the number and orientation of MNWs (Fig. 2(a)), the reaction wells were removed and some particles of PDMS also observed on the sensor surface (Fig. 2(a)). Here, six sensors with welldispersed MNWs were selected, three of which (sensor A1, A3 and B4) were passivated with 33 nm oxide layers, and the others (sensor B7, C7 and D7) were passivated with 500 nm SiO₂. Fig. 2(b) shows the real-time sensor signal for the selected sensors. Ni MNWs were added at 8 min. As the solvent evaporated, the average distance between MNWs and the sensor surface was reduced, which led to an increase in the sensor signal. After the solvent fully evaporated, the MNWs settled onto the surface with minimum movement. At this point, the sensor signals stabilized. The fluctuations of the signal were likely due to some minor movements of the MNWs under the influence of the applied magnetic field as well as the noise of the handheld system. A negative control experiment was performed by adding only ethanol to the sensor surface (Fig. S3). To validate the capability of the GMR sensors in detecting MNWs in aqueous solution, the sensor signal for the detection of MNWs in DI water is also shown in Fig. S4.

There are two ways to implement biomarker detection based on GMR sensors and MNWs. First, a target molecule can be collected on the sensors such that specifically-labeled MNWs attach to these molecules for magnetic detection. This method is appropriate for low concentrations (early detection) of target molecules. In another method, the MNWs can be used to label molecules or cells [24,33] in an assay, unattached MNWs are rinsed away, and the remaining MNWs are detected by GMR sensors. Note that in cell studies, the cells themselves are no longer needed after rinsing, because any remaining magnetic signal is from a once-attached MNW that will be closer to the sensor than if it was still inside a cell. Future studies, therefore, could break cell membranes after rinsing but before adding assay to the reaction well for detection of very low concentrations. In both cases, the sensor signal should exhibit monotonous correlation to the target concentration, which makes the number of MNWs proportional to the number of target molecules or cells.

To explore the factors influencing sensor signal, the number and orientation of MNWs was obtained by SEM, after the sensor signal was calculated from the real-time measurement. The sensor signal was found to increase with increased number of MNWs and decreased passivation layer thickness, as shown in Fig. 2(c), which demonstrates MNWs' potential of serving as magnetic tags in biomarker detection. Moreover, the GMR sensors were able to detect as few as 6 MNWs, which is 2500 times less than the detectable number of iron oxide magnetic nanobeads assuming 150 magnetic nanobeads contribute to 1 ppm of the sensor signal [34]. MNWs are larger than MNPs, but they maintain single-domain ferromagnetic behavior, resulting inhigh stray fields, which make MNWs promising in detecting target molecules with

ultra-low concentration. In addition to the number of MNWs and the distance to the sensor surface, the angle between the long axis of the MNWs and the sensor stripes can also contribute to the sensor signal due to the highly anisotropic magnetic properties of the MNWs. This angular dependence will be discussed in the next section.

3.2. Sensor signal calculation

The calculated stray field from Ni MNWs is shown in Fig. 3 assuming the MNWs were uniformly magnetized with the saturation magnetization of 6100 Gauss. The MNW employed in the calculation was cylindrical with a diameter of 120 nm and a length of 24 μm . The MNW stray field in the direction perpendicular to the long axis was highly localized at both ends of the MNW. As is shown in Fig. S5, the equilibrium state of the MNW at remanence was a single domain with magnetization along the long axis. The ends of the MNW, however, exhibited a vortex-like spin configuration where the magnetization points off the long axis. Due to the negligible stray field from the middle of the MNWs, only the contribution from the ends of the MNWs was considered, which made the sensor signal independent of the variation in the length of the MNWs. In addition, the v component of the stray field decayed from 170 Oe (13.5 kA/m) at a distance of 100 nm to 2 Oe (0.16 kA/m) at $1 \mu m$ and 0.5 Oe (0.04 kA/m) at $2 \mu m$ (Fig. 3(a)(b)). Z component of the stray field also experienced similar decay (Fig. 3(c)(d)). The fast decay of the stray field with increased distance from MNWs to sensor surface indicated that only the MNWs in proximity to the sensor stripes contributed to the sensor signal, which was verified by Fig. 2(c). Consequently, the acquired sensor signal only depended on the number of MNW ends that lie around the sensor stripes and the angle of the MNWs with respect to the sensor stripes. Since both the number and the angle of the MNWs could be determined by the SEM images after the detection process, the total sensor signal was calculated and compared with the experimental results.

To acquire better SEM images for sensor signal calculation, MNW aggregation and the influence from irrelevant particles should be minimized. To accomplish thisa new study was conducted without reaction wells to eliminate the PDMS particles, Fig. 4(a)-(c). The ethanol evaporation rate also increased, which reduced the movement of MNWs on the sensor surface, thus minimizing the MNW aggregation and signal fluctuation. The real-time sensor signal from the GMR sensors is shown in Fig. 4(d). Several assumptions were made to simplify the signal calculation. Firstly, since the coercivity of the MNWs (5000 Oe, 397.9 kA/m) was much larger than the employed magnetic field in the biological detection process (30 Oe, 2.39 kA/m), the longitudinal component of the applied field with respect to the MNWs did not change the stray field from the MNWs. Secondly, only the MNW stray field component that was along the short axis of the sensor stripe contributed to the sensor signal, which is also due to the large shape anisotropy of the sensor stripe. The longitudinal component of the MNW stray field stayed constant under different applied field, thus it didn't contribute to the change of the sensor MR. Thirdly, if the end of a MNW was more than $2 \, \mu m$ away from the sensor stripe, it did not contribute to the sensor signal.

During this study, the applied magnetic field was always along the short axis of the sensor stripe. As shown in the inset of Fig. 4(e), if the angle between the MNW and the applied magnetic field is θ , the stray field perpendicular to MNW's long axis $(H_{d\perp})$ is proportional to the perpendicular component of the applied magnetic field $(H_{a\perp})$ [33], which can be written as

$$H_{d\perp} = cH_{a\perp} = cH_a \sin\theta \tag{2}$$

where c is the proportionality constant. Since the GMR sensor was only sensitive to the field along its short axis, the effective demagnetization field from the MNW (ΔH) can be expressed as

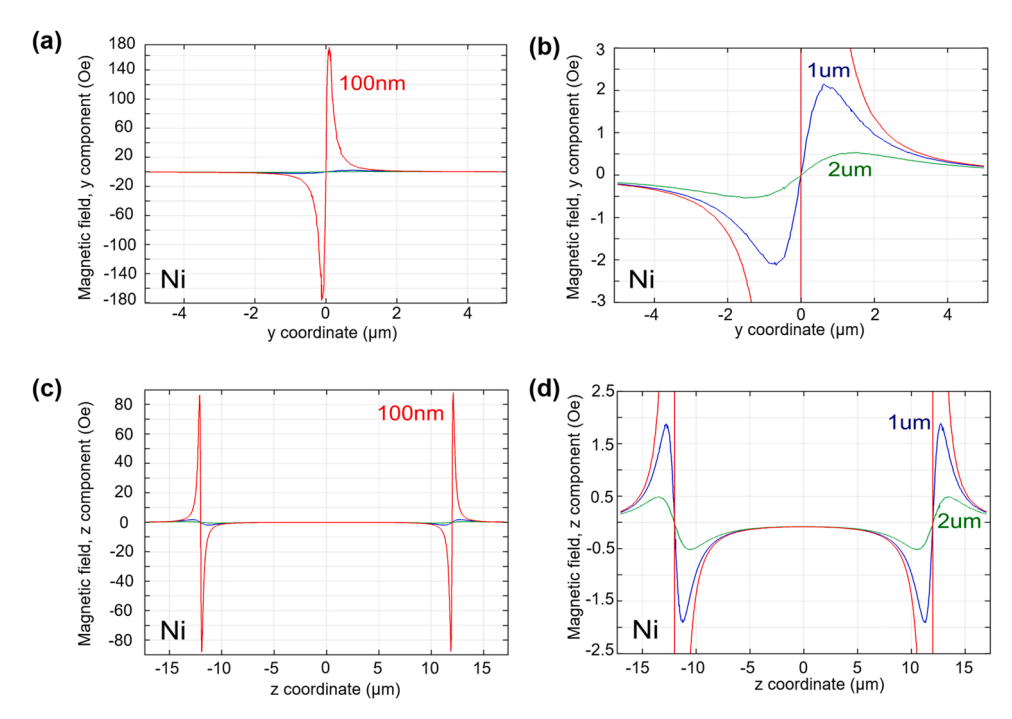


Fig. 3. Distribution of the y component (a, b) and z component (c, d) of the stray field calculated at distances of 100 nm, $1 \mu m$ and $2 \mu m$. To better illustrate the field distribution for the distances of $1 \mu m$ and $2 \mu m$, the middle parts of (a) and (c) are zoomed in and shown in (b) and (d), respectively. The direction of y and z axis with respect to the geometry of the sensor is presented in Fig. 2(a).

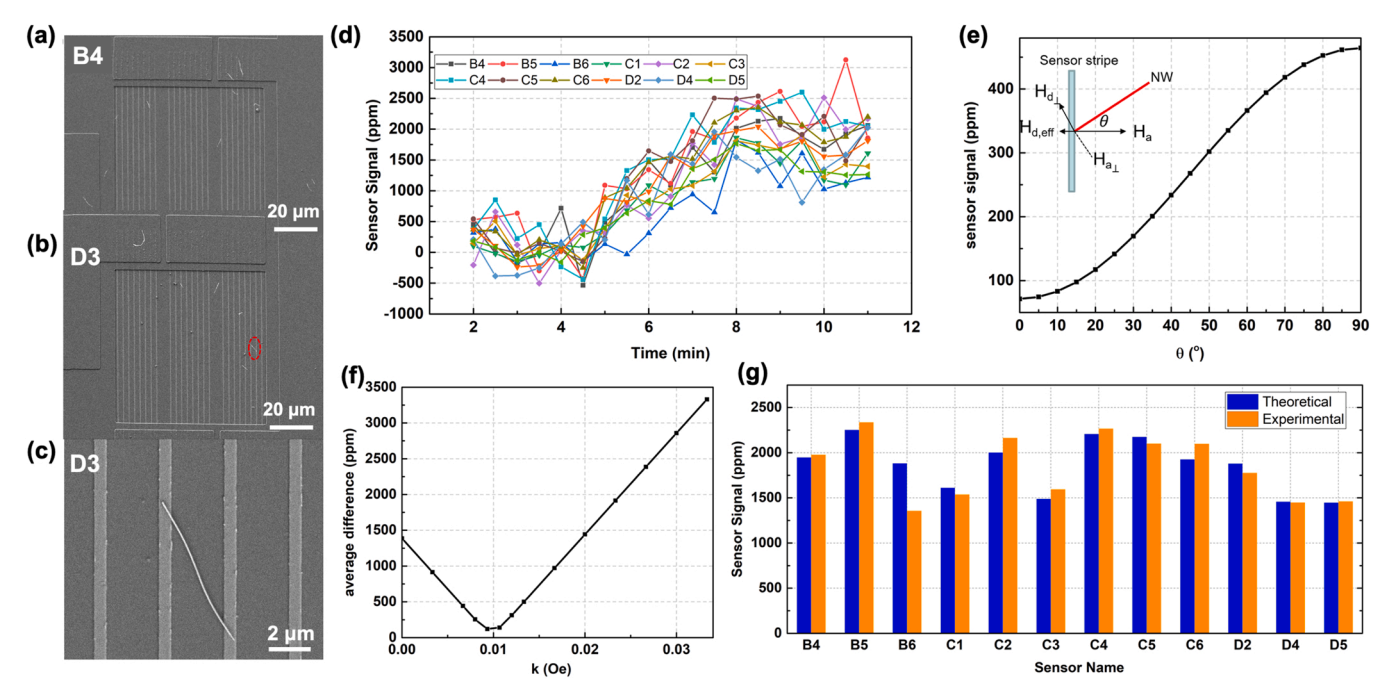


Fig. 4. (a)(b) SEM images of sensors for sensor B4 and D3 with MNWs. (c) SEM image of the MNW in the red circle from (b). (d) Real-time GMR sensor signal after the addition of MNW solution. (e) Sensor signal dependence on the angle between the long axis of the nanowire and the sensor short axis. The denotations are shown in the inset. (f) The average difference between the theoretical and experimental sensor signal for different k values. (g) Comparison between theoretical and experimental results of sensor signal for different sensors for k = 0.009.

$$\Delta H = kH_a \sin^2 \theta \tag{3}$$

$$k = k_0 c \tag{4}$$

where k_0 is a constant that relates to various factors in the sensing scheme, which will be discussed later. The sensor signals induced by ΔH can be derived from the RH loop of the GMR sensor, which can be

$$S = \frac{\Delta MR}{MR_0} = \frac{1}{24} \left(\frac{2R_2 \left(1 - k \sin^2 \theta \right)}{(R_1 - R_2) \left(k \sin^2 \theta - 1 \right) + 2R_0} - 1 \right)$$
 (5)

where R_1 , R_0 , and R_2 are the sensor resistance under the applied field of - 30 Oe (-2.39 kA/m), 0 kA/m and 30 Oe (2.39 kA/m) in the absence

of the MNWs, respectively. The detailed derivation process can be found in Section 6, Supplementary Information. Based on the above equation, the sensor signal was calculated for each of the GMR sensors by adding up the signal for all the MNWs landing on the sensor surface. It is worth mentioning that k_0 is the correction factor that takes the non-uniformity of the demagnetization field into account. It was assumed that a uniform effective demagnetization field was experienced by the sensor, which is the demagnetization field from the surface of the MNW multiplied by k_0 . The optimum k value was found for subsequent calibration of the sensor/MNW system by calculating the average difference between the theoretical and experimental values for all the sensors, as is shown in Fig. 4(f). The minimum average difference of 120 ppm was achieved at k = 0.009. This difference was within the noise level (200 ppm) of the sensing platform, indicating a good fit of the model with the experimental results. Fig. 4(e) shows the sensor signal variation when the MNWs were lying in different angles with respect to the applied field, which verified that unlike isotropic magnetic nanotags, angular dependence should be considered for MNWs. The theoretical and experimental sensor signal for each of the sensors are shown in Fig. 4(g).

3.3. Cell detection with MNWs as nanotags

OSCA-8 cells were chosen for a proof of concept to use MNWs as magnetic nanotags for GMR-based cellular biosensing. As described in

the Experimental section above, the MNW-loaded OSCA-8 cells were fixed and then dried in ethanol. These fixed/dried cells were dispersed in PBS for sensing. In addition, because ethanol evaporates quickly and cleanly, some cells were magnetically-collected from the PBS and redispersed in ethanol in order to better observe these cells on GMR sensor surfaces for verification. SEM images were taken after the evaporation of ethanol (Fig. 5(a-d)). Cells within the size range of 10–20 µm were observed both within (Fig. 5(a)) and outside (Fig. 5(b)) the sensor regions. As shown in several previous studies [3,23,24] and, the MNWs were internalized by the OSCA-8 cells (Fig. 5(e, f)). C, O, Al, Si peaks in the EDS originated from the carbon coating for SEM imaging and the passivation layers on the sensor surface, respectively. The spatial distributions of different elements are shown in Fig. 5(g-i). It is observed in Fig. 5(g) that although some Ni MNWs are inside the cells, most of them are located on the cell membrane. Another reason that could lead to the low abundance of Ni within the cells is that the energy of the incident beam in EDS is not enough to penetrate the cell membranes. Besides the aforementioned elements. Na and Cl are also found in the cell clusters. which are originated from the NaCl crystals on the cell surface in Fig. 5 (d) as indicated by their spatial distributions in Fig. 5(h) and Fig. 5(i).

Real-time detection of fixed cells dispersed in PBS was demonstrated for cell concentrations of 5×10^4 cells/ml, 2×10^5 cells/ml, 2.5×10^5 cells/ml, 3.3×10^5 cells/ml (Fig. 6(a)). The baseline of the sensor signal was obtained first, followed by the addition of 20 μ L cell sample onto the

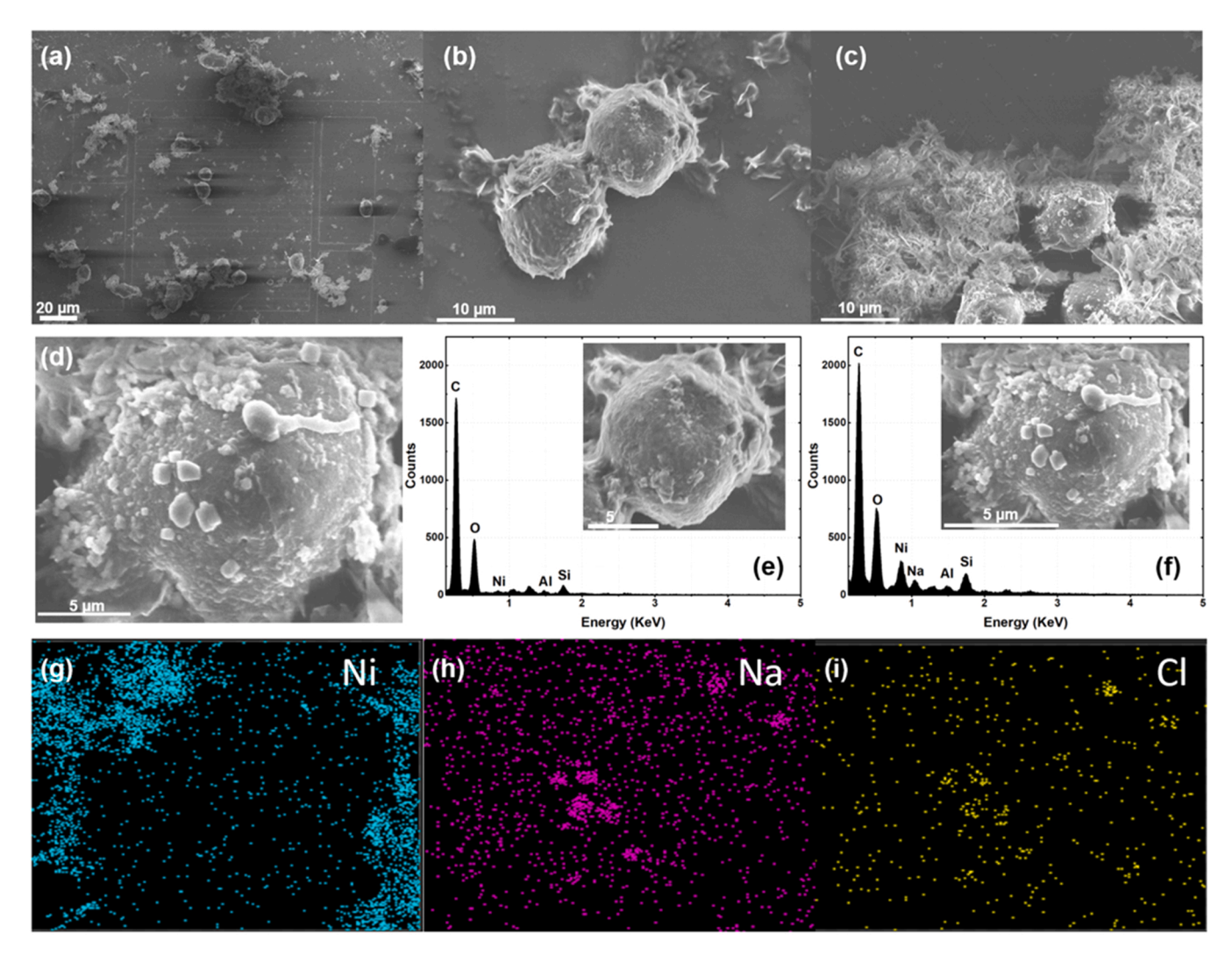


Fig. 5. SEM images of (a) cells on top of a GMR sensor surface, (b) two cells outside the sensor region, (c) a cluster of cells on top of a GMR sensor surface, and (d) surface of one single cell from (c). EDS analysis of the cells in (b) and (c) are shown in (e) and (f), respectively. The spatial distributions of Ni, Na and Cl in the cell displayed in (d) are shown in (g), (h) and (i), respectively.

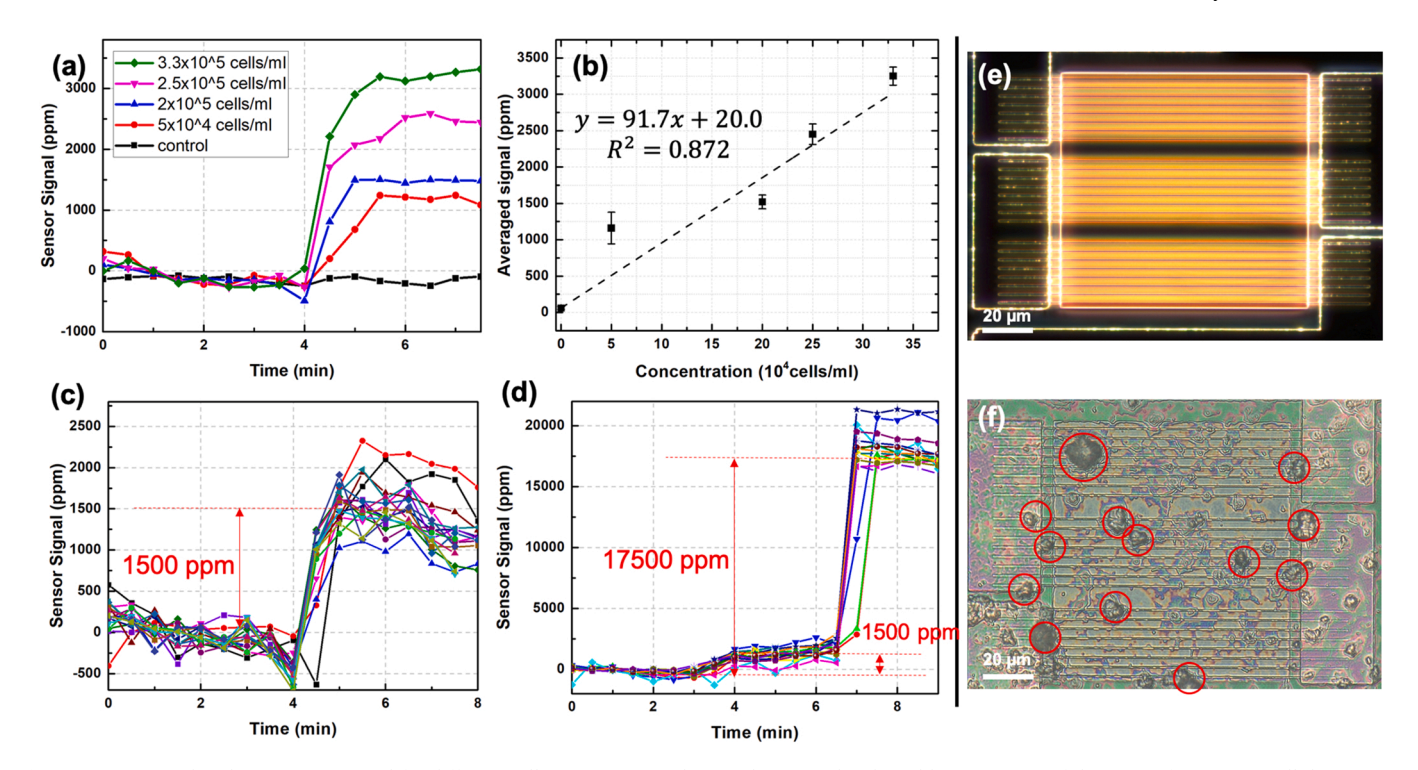


Fig. 6. (a) Averaged real-time sensor signal for different cell concentrations dispersed in PBS. (b) The calibration curve of the sensor for OSCA-8 cell detection in aqueous solutions generated from the saturation signal at different cell concentrations. The error bar is generated from the standard deviation of sensor signal after saturation. Real-time sensor signal for the detection of cells in PBS (c) and ethanol (d) at the concentration of 2×10^5 cells/ml. The plots in different colors indicate the sensor signal from each of the individual sensors on the chip. The optical images of the sensor surface before (e) and after (f) the addition of the sample with cells in ethanol. The cells are highlighted with red circles.

sensor surface at 4 min. The sensor signals increased upon sample addition and reached saturation when the movement of the cells near sensor surface reached equilibrium. The calibration curve of the sensor for the cell detection is shown in Fig. 6(b), where the averaged saturation signal increased with the cell concentration from 1160 ppm at 5×10^4 cells/ml to 3251 ppm at 3.3×10^5 cells/ml. The noise level of the control sensor was 60 ppm. Taking the limit of detection (LOD) as the cell concentration that generated a signal twice as large as the noise level (120 ppm), the LOD for NW-loaded OSCA-8 cells in aqueous solution was calculated to be 6648 cells/ml or 133 cells in a sample volume of 20 μL . Since the stray field from the NWs decayed rapidly with the distance to the sensor surface, the sensor signal generated from cells suspended in the aqueous solution should be much lower than that generated from cells directly located on sensor surface via either evaporation of solvents or chemical bonding.

To explore the signal generated by the cells in direct contact with the sensors, OSCA-8 cells were magnetically collected, re-dispersed in ethanol (2×10^5 cells/ml), and dropped onto the sensor surfaces. For comparison, both the real-time detection results in PBS and ethanol at the same cell concentration are shown in Fig. 6(c) and Fig. 6(d), respectively. The signal from each individual sensor on the chip is shown in different colors. Unlike the sensor signals from the PBS-based samples, which saturated after ~5 min, the sensor signals from ethanolbased samples saturated at 4 min when the surface tension held the ethanol droplets on the sensor surface. After that, the signal increased suddenly as all the cells settled onto the sensor surface with the evaporation of the ethanol. The average number of cells on each sensor can be estimated from the area of the sample spot on the chip (4.9 mm²), the area of each individual sensor (0.0159 mm²), and the total number of cells in the sample (4000), which equals 13 cells per sensor. To validate the calculation, optical images of the GMR chips before (Fig. 6(e)) and after (Fig. 6(f)) cell detection were used for the cell counting. The average number of cells on the sensor surface from 12 sensors with welldispersed cells was 15, which is close to the calculated cell number. The average sensor signal generated from one cell in direct contact with the sensor surface was calculated as the average saturation signal after 7 min in Fig. 6(f) divided by the average number of cells on each sensor, resulting in 1066 ppm/cell, which is well above the noise level of the sensor (60 ppm). It is worth noting that the noise level for cell detection (60 ppm) was lower than that for the MNW detection (200 ppm) due to the employment of reaction wells and lower evaporation rate of the solvent. This indicates that through approaches such as chemical bonding, the GMR sensors will be capable of single cell detection because the cells will be in direct contact with the sensor surface. It is worth mentioning that although the detection performance had negligible angular dependence at the concentrations used here, additional approaches like the application of a gradient magnetic field may be needed for effective single-cell detection.

4. Conclusions

In this paper, we demonstrated the detection of MNW-OSCA-8 cells with GMR sensors for the first time. Various factors influenced the sensor signal, including the distance between the MNW and the sensor surface, the properties of the MNW material, and the number of MNWs on the sensor surface. It was found that the sensor signal contributed by a single MNW was 2500 times larger than the sensor signal from a single magnetic iron oxide nanobead, which indicates MNW have potential for the detection of biomarkers at ultra-low concentrations. Most of the stray fields originated from the end of the MNWs, and they decayed rapidly with distance. These features are independent of MNW length since the MNWs are more than 10x the diameters. Due to the shape anisotropy of both the MNW and the sensor stripes, the sensor signal varied with the angle between the nanowire and the applied field direction for single MNW detection. Using modeling and proper calibration, the average difference between the theoretical and experimental sensor signals was

within the noise level of the system. Finally, the capability of GMR-based cell detection with MNWs as nanotags was demonstrated for the first time with a LOD of 133 cells in 20 μL aqueous solutions and single cell detection when the cells were in direct contact with the sensor surface. The detection time, linearity and cost are comparable to previous works based on the same GMR sensors and the handheld system [30,31]. The cells were collected magnetically, which shows that MNW tags eliminate the need to functionalize additional labels on the cell surface, and this will simplify the detection process and reduce the risk of cell contamination from additional chemical functionalization. The capability of single-cell detection based on our platform possesses great potential in the early diagnosis of circulating tumor cells, which requires a minimum LOD of 1 cell/ml [35], and can be hardly achieved by the current biosensing technologies (>10 cells/ml) [36,37].

CRediT authorship contribution statement

The detection of MNWs with the cells by GMR platform was performed by Diqing Su. The fabrication of GMR sensors was performed by Diqing Su, Kai Wu and Junyang Chen. The MNWs are synthesized by Joseph Um, Zohreh Nemati, Julian Moreno, M. Reza Zamani Kouhpanji and Daniel Shore. The characterization of the GMR sensors and the MNWs were performed by Diqing Su and Karthik Sirnivasan. The experiments were supervised by Professors Jürgen Kosel, Jaime F. Modiano, Rhonda Franklin, Jian-Ping Wang, and Bethanie Stadler.

Declaration of Competing Interest

Dr. Jian-Ping Wang has equity and royalty interests in, and serves on the Board of Directors, for Zepto Life Technology LLC, a company involved in the commercialization of GMR Biosensing technology. The University of Minnesota also has equity and royalty interests in Zepto Life Tech LLC. These interests have been reviewed and managed by the University of Minnesota in accordance with its Conflict of Interest policies.

Data Availability

Data will be made available on request.

Acknowledgement

This work was supported by MNDrive: OVPR STEMMA program, Institute of Engineering in Medicine of the University of Minnesota, National Science Foundation MRSEC facility program, the Distinguished McKnight University Professorship, Centennial Chair Professorship, Robert F Hartmann Endowed Chair, Alvin and June Perlman Endowed Chair in Animal Oncology, the Skippy Frank Fund for Life Sciences and Translational Research, Morris Animal Foundation Grant D15CA-047, the Animal Cancer Care and Research Program of the University of Minnesota, and UROP program from the University of Minnesota. Support was also provided by the King Abdullah University of Science and Technology (KAUST) Office of Sponsored Research (OSR) under Award No. OSR-2016-CRG5-2956. We also acknowledge XPRIZE Foundation and Nokia Sensing XCHALLENGE competition for motivating the design of the Z-Lab Diagnosis Platform which won Distinguished Prize Award. Portions of this work were conducted in the Minnesota Nano Center, which is supported by the National Science Foundation through the National Nano Coordinated Infrastructure Network (NNCI) under Award Number ECCS-1542202. Parts of this work were carried out in the Characterization Facility, University of Minnesota, a member of the NSF-funded Materials Research Facilities Network (www.mrfn.org) via the MRSEC program.

Appendix A. Supporting information

Supplementary data associated with this article can be found in the online version at doi:10.1016/j.sna.2022.114115.

References

- [1] J.H. Huang, X. Gao, J.J. Jia, J.K. Kim, Z.G. Li, Graphene oxide-based amplified fluorescent biosensor for Hg²⁺ detection through hybridization chain reactions, Anal. Chem. 86 (6) (2014) 3209–3215.
- [2] X.R. Wang, J.M. Hu, G.Y. Zhang, S.Y. Liu, Highly selective fluorogenic multianalyte biosensors constructed via enzyme-catalyzed coupling and aggregation-induced emission, J. Am. Chem. Soc. 136 (28) (2014) 9890–9893.
- [3] D. Rodrigo, O. Limaj, D. Janner, D. Etezadi, F.J.G. de Abajo, V. Pruneri, H. Altug, Mid-infrared plasmonic biosensing with graphene, Science 349 (6244) (2015) 165–168.
- [4] X.J. Yang, Y.B. Yu, Z.Q. Gao, A highly sensitive plasmonic DNA assay based on triangular silver nanoprism etching, Acs Nano 8 (5) (2014) 4902–4907.
- [5] C.A. Heid, J. Stevens, K.J. Livak, P.M. Williams, Real time quantitative PCR, Genome Res. 6 (10) (1996) 986–994.
- [6] J.Y. Shi, C.Y. Chan, Y.T. Pang, W.W. Ye, F. Tian, J. Lyu, Y. Zhang, M. Yang, A fluorescence resonance energy transfer (FRET) biosensor based on graphene quantum dots (GQDs) and gold nanoparticles (AuNPs) for the detection of mecA gene sequence of Staphylococcus aureus, Biosens. Bioelectron. 67 (2015) 595–600.
- [7] V.D. Krishna, K. Wu, A.M. Perez, J.P. Wang, Giant magnetoresistance-based biosensor for detection of Influenza A virus, Front. Microbiol. 7 (2016) 8.
- [8] J. Schotter, P.B. Kamp, A. Becker, A. Puhler, G. Reiss, H. Bruckl, Comparison of a prototype magnetoresistive biosensor to standard fluorescent DNA detection, Biosens. Bioelectron. 19 (10) (2004) 1149–1156.
- [9] D.R. Baselt, G.U. Lee, M. Natesan, S.W. Metzger, P.E. Sheehan, R.J. Colton, A biosensor based on magnetoresistance technology, Biosens. Bioelectron. 13 (7–8) (1998) 731–739.
- [10] D.L. Graham, H. Ferreira, J. Bernardo, P.P. Freitas, J.M.S. Cabral, Single magnetic microsphere placement and detection on-chip using current line designs with integrated spin valve sensors: Biotechnological applications, J. Appl. Phys. 91 (10) (2002) 7786–7788.
- [11] S.J. Osterfeld, H. Yu, R.S. Gaster, S. Caramuta, L. Xu, S.J. Han, D.A. Hall, R. J. Wilson, S.H. Sun, R.L. White, R.W. Davis, N. Pourmand, S.X. Wang, Multiplex protein assays based on real-time magnetic nanotag sensing, Proc. Natl. Acad. Sci. USA 105 (52) (2008) 20637–20640.
- [12] D.Q. Su, K. Wu, R. Saha, C.Y. Peng, J.P. Wang, Advances in magnetoresistive biosensors. Micromachines 11 (2020) 1.
- [13] B. Srinivasan, Y.P. Li, Y. Jing, Y.H. Xu, X.F. Yao, C.G. Xing, J.P. Wang, A detection system based on giant magnetoresistive sensors and high-moment magnetic nanoparticles demonstrates zeptomole sensitivity: potential for personalized medicine, Angew. Chem. -Int. Ed. 48 (15) (2009) 2764–2767.
- [14] Z. Chu, M. Fu, J. Guo, W. Wang, J. Zhou, X. Ma, J. Guo, Magnetic resistance sensory system for the quantitative measurement of morphine, IEEE Trans. Biomed. Circuits Syst. 15 (1) (2021) 171–176.
- [15] G. Yang, K. Cheng, Z. Chu, C. Ren, Y. Fu, J. Guo, A miniaturized giant magnetic resistance system for quantitative detection of methamphetamine, Analyst 146 (8) (2021) 2718–2725.
- [16] S.X. Wang, G. Li, Advances in giant magnetoresistance biosensors with magnetic nanoparticle tags: review and outlook, IEEE Trans. Magn. 44 (7) (2008) 1687–1702.
- [17] W. Wang, Y. Jing, S.H. He, J.P. Wang, J.P. Zhai, Surface modification and bioconjugation of FeCo magnetic nanoparticles with proteins, Colloids Surf. B-Biointerfaces 117 (2014) 449–456.
- [18] K. Bente, A. Codutti, F. Bachmann, D. Faivre, Biohybrid and bioinspired magnetic microswimmers, Small 14 (29) (2018) 25.
- [19] O. Yassine, A. Zaher, E.Q. Li, A. Alfadhel, J.E. Perez, M. Kavaldzhiev, M. F. Contreras, S.T. Thoroddsen, N.M. Khashab, J. Kosel, Highly efficient thermoresponsive nanocomposite for controlled release applications, Sci. Rep. 6 (2016).
- [20] C. Naud, C. Thébault, M. Carrière, Y. Hou, R. Morel, F. Berger, B. Dieny, H. Joisten, Cancer treatment by magneto-mechanical effect of particles, a review, Nanoscale Adv. 2 (2020) 3632–3655.
- [21] A. Hultgren, M. Tanase, C.S. Chen, D.H. Reich, High-yield cell separations using magnetic nanowires, IEEE Trans. Magn. 40 (2004) 2988–2990.
- [22] H.T. Huang, T.R. Ger, Y.H. Lin, Z.H. Wei, Single cell detection using a magnetic zigzag nanowire biosensor, Lab Chip 13 (15) (2013) 3098–3104.
- [23] D.E. Shore, T. Dileepan, J.F. Modiano, M.K. Jenkins, B.J.H. Stadler, Enrichment and quantification of epitope-specific CD4+T lymphocytes using ferromagnetic iron-gold and nickel nanowires, Sci. Rep. (2018) 8.
- [24] A. Sharma, G.M. Orlowski, Y.C. Zhu, D. Shore, S.Y. Kim, M.D. DiVito, A. Hubel, B.J. H. Stadler, Inducing cells to disperse nickel nanowires via integrin-mediated responses, Nanotechnology 26 (2015) 13.
- [25] T.S. Ramulu, R. Venu, B. Sinha, S.S. Yoon, C.G. Kim, Electrodeposition of CoPtP/Au multisegment nanowires: synthesis and DNA functionalization, Int. J. Electrochem. Sci. 7 (9) (2012) 7762–7769.
- [26] L.P. Felix, J.E. Perez, M.F. Contreras, T. Rayasi, J. Kosel, Cytotoxic effects of nickel nanowires in human fibroblasts, Toxicol. Rep. 3 (2016) 373–380.

- [27] M.B. Margineanu, K. Julfakyan, C. Sommer, J.E. Perez, M.F. Contreras, N. Khashab, J. Kosel, T. Ravasi, Semi-automated quantification of living cells with internalized nanostructures, J. Nanobiotechnol. (2016) 14.
- [28] S.M. Reddy, J.J. Park, S.M. Na, M.M. Maqableh, A.B. Flatau, B.J.H. Stadler, Electrochemical synthesis of magnetostrictive Fe-Ga/Cu multilayered nanowire arrays with tailored magnetic response, Adv. Funct. Mater. 21 (24) (2011) 4677–4683.
- [29] M.M. Maqableh, X.B. Huang, S.Y. Sung, K.S.M. Reddy, G. Norby, R.H. Victora, B.J. H. Stadler, Low-resistivity 10 nm diameter magnetic sensors, Nano Lett. 12 (8) (2012) 4102–4109.
- [30] D.Q. Su, K. Wu, V.D. Krishna, T. Klein, J.M. Liu, Y.L. Feng, A.M. Perez, M.C. J. Cheeran, J.P. Wang, Detection of influenza a virus in swine nasal swab samples with a wash-free magnetic bioassay and a handheld giant magnetoresistance sensing system, Front. Microbiol. 10 (2019).
- [31] K. Wu, T. Klein, V.D. Krishna, D.Q. Su, A.M. Perez, J.P. Wang, Portable GMR handheld platform for the detection of Influenza A virus, ACS Sens. 2 (11) (2017) 1504–1601
- [32] A. Anguelouch, D.H. Reich, C.L. Chien, M. Tondra, Detection of ferromagnetic nanowires using GMR sensors, IEEE Trans. Magn. 40 (4) (2004) 2997–2999.
- [33] A. Sharma, Y.C. Zhu, S. Thor, F. Zhou, B. Stadler, A. Hubel, Magnetic barcode nanowires for osteosarcoma cell control, detection and separation, IEEE Trans. Magn. 49 (1) (2013) 453–456.
- [34] R.S. Gaster, L. Xu, S.-J. Han, R.J. Wilson, D.A. Hall, S.J. Osterfeld, H. Yu, S. X. Wang, Quantification of protein interactions and solution transport using high-density GMR sensor arrays, Nat. Nanotechnol. 6 (5) (2011) 314–320.
- [35] Y.P. Ivanov, M. Vazquez, O. Chubykalo-Fesenko, Magnetic reversal modes in cylindrical nanowires, J. Phys. D. -Appl. Phys. 46 (48) (2013) 11.
- [36] X. Hu, X. Zang, Y. Lv, Detection of circulating tumor cells: advances and critical concerns, Oncol. Lett. 21 (2021), 1-1.
- [37] E. Racila, D. Euhus, A.J. Weiss, C. Rao, J. McConnell, L.W. Terstappen, J.W. Uhr, Detection and characterization of carcinoma cells in the blood, Proc. Natl. Acad. Sci. 95 (1998) 4589–4594.

Diqing Su is a PhD student at University of Minnesota in the department of Chemical Engineering and Materials Science. She is currently working on GMR biosensing and the fabrication of flexible magnetic sensors.

Joseph Um currently works as a PhD student at the Department of Electrical and Computer Engineering, University of Minnesota Twin Cities. He is currently working on the synthesize and characterization of magnetic nanowires.

Julian Moreno is a Ph.D. student in Sensing, Magnetism and Microsystems (SMM) Research group at King Abdullah University of Science and Technology (KAUST). He is currently working on magnetic nanowires and other magnetic nanomaterials.

Zohreh Nemati currently works as a postdoctoral researcher at the Department of Electrical and Computer Engineering, University of Minnesota Twin Cities on the synthesize and characterization of magnetic nanomaterials.

Karthik Srinivasa currently works as a PhD student at the Department of Electrical and Computer Engineering, University of Minnesota Twin Cities. He is currently working on the synthesize and characterization of magnetic nanowires.

Junyang Chen currently works as a postdoctoral researcher at the Department of Electrical and Computer Engineering, University of Minnesota Twin Cities on magnetic tunnel junctions and magneto-optical devices.

M. Reza Zamani Kouhpanji currently works as a PhD student at the Department of Electrical and Computer Engineering, University of Minnesota Twin Cities. He is currently working on the synthesize and characterization of magnetic nanowires.

Daniel Shore is a PhD student at University of Minnesota in the department of Chemical Engineering and Materials Science. He is currently working on the synthesize and characterization of magnetic nanowires.

Kai Wu works as a postdoctoral researcher at the Department of Electrical and Computer Engineering, University of Minnesota Twin Cities. He is currently working on novel magnetic biosensors.

Professor Jürgen Kosel currently works at Electrical and Computer Engineering. Head of Sensing Magnetism and Microsystems Group, King Abdullah University of Science and Technology (KAUST). His research interests are in the field of micro- and nano devices with special emphasis on magnetic effects.

Professor Jaime F. Modiano works at the Department of Veterinary Clinical Sciences, University of Minnesota, Twin cities. The focus of his research has been to understand cell growth regulation in the context of cancer pathogenesis, fostering an environment that spans basic to translational research.

Rhonda Franklin is a Professor of Electrical and Computer Engineering at the University of Minnesota. She is a microwave and radio frequency engineer whose research focuses on microelectronic mechanical structures in radio and microwave applications.

Professor Jian-Ping Wang currently works at the Department of Electrical and Computer Engineering, University of Minnesota Twin Cities. His research focuses on Nano magnetic and spintronic materials and devices, magnetic and spintronic information storage and computing technologies, magnetic biomedical technologies.

Professor Bethanie Stadler currently works at the Department of Electrical and Computer Engineering, University of Minnesota Twin Cities. Her research focuses on Magnetic nanowire arrays for high density RAM, nanowire RFID tags for cells, and integrated photonics